Green functions for multiple scattering as mathematical tools for dense-cloud remote sensing: Theory, with passive and active applications

Anthony B. Davis*[a], Alexander Marshak**[b], and Robert F. Cahalan[c]
[a]Los Alamos National Laboratory, Space and Remote Sensing Sciences Group (NIS-2);
[b]University of Maryland - Baltimore County, Joint Center for Earth-science Technology;
[c]NASA - Goddard Space Flight Center, Climate and Radiation Branch (Code 913).

ABSTRACT

We survey radiative Green function theory (1) in linear transport theory where numerical procedures are required to obtain specific results and (2) in the photon diffusion limit (large optical depths) where it is analytically tractable, at least for homogeneous plane-parallel media. We then describe two recent applications of Green function theory to passive cloud remote sensing in the presence of strong three-dimensional transport effects. Finally, we describe recent instrumental breakthroughs in "off-beam" cloud lidar which is based on direct measurements of radiative Green functions with special attention to the data collected during the Shuttle-based Lidar In-space Technology Experiment (LITE) mission.

Keywords: Green functions, radiative transfer, multiple scattering, photon diffusion, optical tomography, laser remote sensing, cloud remote sensing.

1. INTRODUCTION

In mathematical physics, Green functions are the so-called fundamental solutions of linear PDE systems, i.e., with Dirac δ-functions as source terms. In optics, pulsed lasers are excellent operational realizations of δ-function sources in photon state-space: position, time, wavelength (or energy), propagation direction (or momentum), and even polarization. The response of a scattering medium to a laser pulse is therefore a physical manifestation of its radiative transfer Green function. From the angular/spatial standpoint, most lidar observations use only a small fraction of this information, just the directly back-scattered signal. This signal is easy to interpret for optically thin media, for instance, the cloud-free atmosphere but it is quickly lost in the background noise when strong extinction is encountered. Advanced techniques use the resulting excitations in cross-polarization and at Doppler- or Raman-shifted wavelengths. However, directivity and time-dependence are invariably used to obtain the range of the scattering event (or optical "echo").

In atmospheric applications, the standard "on-beam" observation geometry reduces lidar to a cloud detection (ceilometry) device as soon as an optically thick layer appears. By judicious use of polarization,[1] some information about the phase and size-distribution of cloud particles can be obtained within the first layers; however, multiple forward-scattering corrections must be applied.[2] Alternatively or in combination with depolarization, multiple fields-of-view (all in the mrad range) can be used to the same effect.[3] In contrast, emerging "off-beam" lidar techniques fully exploit the available space- and time-dependent radiation fields. Using basic Green function theory, we have shown[4-6] that these multiple-scattering lidar instruments are rudimentary optical tomography[7] tools that can be used to determine a cloud's thickness, density (optical depth), and possibly its degree of internal variability. In this context, the temporal dependence is no longer mapped to range but rather to the cloud-medium's impulse-response, and there is an entirely new angular signal to analyze as well.

The paper is organized as follows. The next section introduces radiative Green functions in general and in two contrasting approximate formulations, one being the standard lidar equation. Section 3 surveys the analytical theory of Green functions for plane-parallel media in the photon diffusion approximation and demonstrates its validity by comparison with numerical solutions of the associated problem in linear transport theory. In section 4, we cover four application areas at different levels of detail: two in passive cloud remote sensing, two for active approaches; a special emphasis is placed on space-borne lidar observations obtained during the NASA's Lidar In-space Technology Experiment (LITE) mission flown on the Space Shuttle in September 1994. We summarize our findings in Section 5 and outline some future work.

* adavis@lanl.gov; phone +1-505-665-6577; fax: +1-505-667-9208; http://nis-www.lanl.gov/~adavis; LANL/NIS-2, P.O. Box 1663 (Mail Stop C-323), Los Alamos, NM, USA 87545; ** marshak@climate.gsfc.nasa.gov; phone +1-301-614-6122; fax: +1-301-614-6307; NASA - GSFC (Code 913), Greenbelt, Md, USA 20771.

Laser Radar Technology and Applications VI, Gary W. Kamerman, Editor,
Proceedings of SPIE Vol. 4377 (2001) © 2001 SPIE · 0277-786X/01/$15.00

2. RADIATIVE GREEN FUNCTIONS, DEFINITION AND APPROXIMATIONS

2.1 The time-dependent radiative transfer equation with Dirac δ-source on a boundary

The schematic in Fig. 1a describes the geometry of radiative Green function (GF) generation for a boundary source and observation (with off-beam cloud lidar). The key quantities are cloud optical depth (τ), physical thickness (H), asymmetry factor of scattering phase function (g), and range (d_{obs}). The remotely observable radiative transfer GFs for a δ-source at the cloud boundary (G_{obs}) will depend parameterically on all of these cloud quantities as well as two independent variables for space and one for time. The spatial variable can be determined in Cartesian coordinates (x,y) measured away from the point-source, cylindrical coordinates (ρ,φ) convenient when the detector is at very large range ($d_{obs} \gg H$), or else polar angles (θ_ρ,φ) when the cloud is at relatively close range (then $\tan\theta_\rho = \rho/d_{obs}$). The temporal variable can be either time elapsed since the pulse impacted the cloud (t), or the "in-cloud" pathlength ($\lambda = ct$), noting that the "out-of-cloud" pathlength is simply $(1+1/\cos\theta_\rho)d_{obs}$. The instrumental parameters that affect non-trivially the observed signal are the beam diameter and pulse width for the transmitter (smoothing of space-time GF), as well as the field-of-view (FOV) of the receiver optics (spatial truncation of the GF).

In time-dependent 3D radiative transfer with no internal sources or sinks, we use the integro-differential equation,

$$\left[c^{-1}\frac{\partial}{\partial t} + \mathbf{\Omega}\bullet\nabla + \sigma(\boldsymbol{r})\right] I = \sigma(\boldsymbol{r}) \int_{\Xi} p(\boldsymbol{r};\mathbf{\Omega}'\bullet\mathbf{\Omega}) I(t,\boldsymbol{r};\mathbf{\Omega}')\mathrm{d}\mathbf{\Omega}', \tag{1}$$

subject to boundary/initial conditions to determine the time-dependent radiance field $I(t,\boldsymbol{r};\mathbf{\Omega})$ at instant $t \geq 0$, and position $\boldsymbol{r} = \{ (x,y,z)^T \in \Re^3 \mid 0 \leq z \leq H \}$, i.e., in a plane-parallel slab medium. The propagation direction $\mathbf{\Omega}$ is a vector on the unit 3-sphere Ξ which can be divided as needed into the up-welling (Ξ_+) and downwelling (Ξ_-) hemispheres. In the non-steady radiative transfer equation or "RTE" in (1), we have used the following notations: c is the speed of light; $\sigma(\boldsymbol{r})$ is the extinction coefficient; and $p(\boldsymbol{r};\mathbf{\Omega}'\bullet\mathbf{\Omega})$ is the scattering phase function, assumed azimuthally symmetric, where $\mathbf{\Omega}'\bullet\mathbf{\Omega} = \cos\theta_S$ is the cosine μ_S of the scattering angle (cf. Fig. 1a). In this study, we use boundary/initial conditions for a collimated point-source pulse at a cloud boundary. For instance, illumination from below is described by

$$I(t,x,y,0;\mathbf{\Omega}(\mu,\phi)) = \delta(t)\delta(x)\delta(y)\delta(\mu-1)/2\pi, \quad \mu > 0; \tag{2a}$$
$$I(t,x,y,H;\mathbf{\Omega}(\mu,\phi)) = 0, \quad \mu < 0. \tag{2b}$$

For a diffuse source, we just replace $\delta(\mu-1)/2\pi$ in (2a) with π^{-1}. In this case, we denote the solution as $G_\partial(t,\boldsymbol{r},\mathbf{\Omega})$ where the subscript "∂" reminds us that the source is at a cloud boundary. We are particularly interested in boundary fluxes, especially in reflection:

$$G_R(t,x,y) = \int_{\Xi_-} |\Omega_z| G_\partial(t,x,y,0;\mathbf{\Omega})\mathrm{d}\mathbf{\Omega} = \int_{\mu\leq 0} |\mu| \left[\int_{2\pi} G_\partial(t,x,y,0;\mathbf{\Omega}(\mu,\phi))\mathrm{d}\phi \right] \mathrm{d}\mu. \tag{3}$$

Figure 1b shows numerical results for a homogeneous slab of optical depth

$$\tau = \sigma H = 16; \tag{4}$$

due to the uniformity of the cloud and the symmetry of the illumination pattern, we have $G_R(t,x,y) \equiv G_R(t,\rho)$. For a realistically variable cloud case, but showing the space-only GF, see ref. 8.

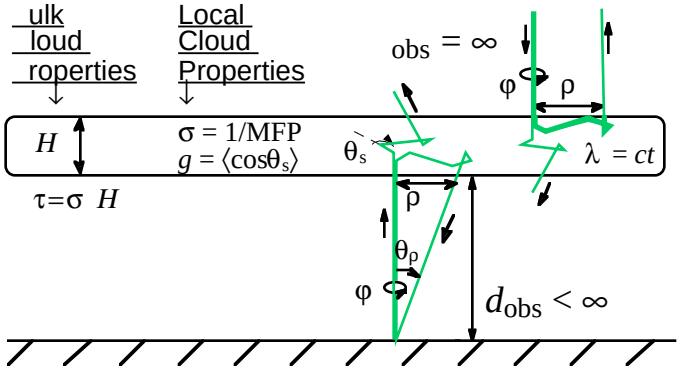

Figure 1a: *Schematic for radaitive Green function generation and observation for a dense cloud layer.* From left to right, illustrated meanings for: (1) cloud optical depth τ, physical thickness H, their ratio (extinction σ), and asymmetry factor g (mean cosine of scattering angle) ≈ 0.85 for typical droplet populations; (2) independent variables angle (space) θ_ρ and time t, radiance $G_{obs}(\tau,g,H,d_{obs};t,\theta_\rho,\varphi)$ for a ground-based WAIL system and a cloud at finite range d_{obs}; (3) similarly, $G_{obs}(\tau,g,H,\infty;t,\rho,\varphi)$ is measured during a LITE-like mission in space. The latter signal has been extensively studied elsewhere[9-11] and will be the subject of §4.4 below.

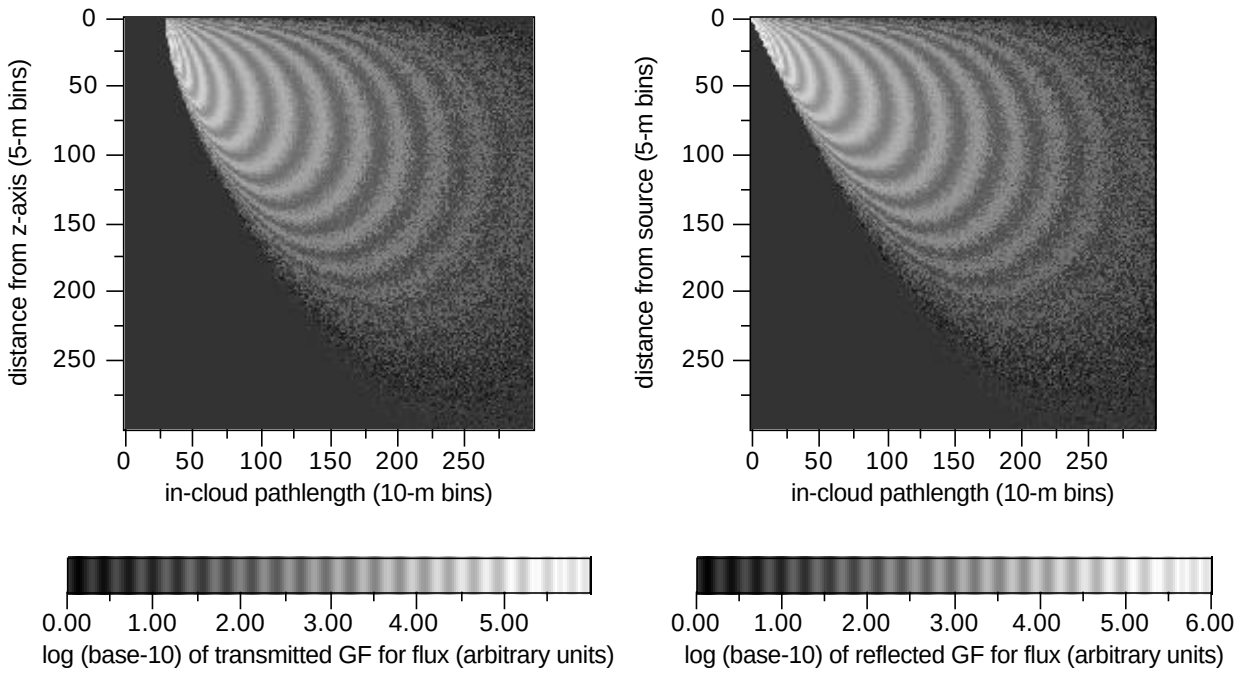

Figure 1b: *Results from numerical (Monte Carlo) computations.* We show Green functions for a homogenous cloud of physical thickness H = 300 m, optical depth τ = 16 and a Henyey-Greenstein[12] scattering phase function with g = 0.85. Illumination is normal and overall albedo is found to be R = 0.557, hence T = 0.443. Left hand side is the transmitted Green function, $G_T(t,\rho)$; right hand side is $G_R(t,\rho)$, for reflection. Notice the different lower envelopes: diffusive ($\rho \propto \sqrt{t\text{-}H/c}$) for T, and ballistic ($\rho \propto t$) for R.

2.2 Optically thin media: The lidar equation as a special solution in the single-scattering limit

The lidar equation predicts the radiant energy E (in units of pulse energy) received by a detector as a function of time t, i.e., from a range $z = ct/2$. For a monostatic zenith-pointing device at $x = y = z = 0$ with an aperture of area A, it reads as

$$E(t=2z/c) = T_d(z)^2 \times c\sigma(0,0,z) \times p(0,0,z;-1)A/z^2, \text{ with } T_d(z) = \exp[-\int_0^z \sigma(0,0,z')dz'] \tag{5}$$

for the ideal pulse and perfect detector. This can be recast in instrument-independent radiometric notations of §2.1 as

$$I(t,\boldsymbol{r}=\boldsymbol{0}) = c\sigma(0,0,ct/2)\, p(0,0,ct/2;-1)\, \exp[-2\int_0^{ct/2} \sigma(0,0,z)dz]. \tag{6}$$

Although a rigorous proof is out of the scope of this paper, (6) is actually the 1st-order scattering solution of the RTE in (1) with boundary/initial conditions (2a-b).

2.3 Optically thick media: The photon diffusion approximation in regimes dominated by multiple-scattering

Diffusion theory is based on highly smoothed versions of the radiance field $I(t,\boldsymbol{r},\boldsymbol{\Omega})$. One key quantity in diffusion theory is photon density

$$U(t,\boldsymbol{r}) = \frac{1}{c} \int I(t,\boldsymbol{r},\boldsymbol{\Omega})\, d\boldsymbol{\Omega}. \tag{7}$$

The other important quantity is the photon flux (or current density) vector

$$\boldsymbol{F}(t,\boldsymbol{r}) = \int \boldsymbol{\Omega} I(t,\boldsymbol{r},\boldsymbol{\Omega})\, d\boldsymbol{\Omega}\ . \tag{8}$$

$U(t,\boldsymbol{r})$ and $\boldsymbol{F}(t,\boldsymbol{r})$ obey two independent constraints. First, they enter the (exact) law of radiant energy conservation:[13]

$$\partial_t U + \boldsymbol{\nabla}\bullet\boldsymbol{F} = 0 \tag{9}$$

in the absence of absorption. Second, they are related by Fick's law for photon diffusion, operating as a constitutive relation that "closes" the transport problem in Eq. (9),

$$\boldsymbol{F}(t,\boldsymbol{r}) = -D(\boldsymbol{r})\boldsymbol{\nabla}U, \tag{10}$$

where $D(\boldsymbol{r})$ is (radiative) diffusivity. We know from kinetic theory (e.g., Rief[14]) that

$$D(\boldsymbol{r}) = c\ell_t(\boldsymbol{r})/3 \tag{11}$$

where $\ell_t(\boldsymbol{r})$ is the transport mean-free-path:

$$\ell_t(\boldsymbol{r}) = 1/\sigma(\boldsymbol{r}) = 1/[(1-g)\sigma(\boldsymbol{r})] \tag{12}$$

where $g = 2\pi\int\mu_S p(\mu_S)d\mu_S$ is the asymmetry factor. In essence, ℓ_t is the "effective" mean-free-path for isotropic scattering.

For $\boldsymbol{r}$-independent extinction, hence diffusivity, Eqs. (9–10) can be combined into a standard parabolic PDE,

$$\partial_t U - D\boldsymbol{\nabla}^2 U = 0, \tag{13}$$

with the following (mixed) boundary/initial conditions for the GF problem at hand:

$$\frac{1}{2}\left[1 - (\chi\ell_t)\frac{\partial}{\partial z}\right]U|_{z=0} = \delta(t)\delta(x)\delta(y); \tag{14a}$$

$$\frac{1}{2}\left[1 + (\chi\ell_t)\frac{\partial}{\partial z}\right]U|_{z=H} = 0. \tag{14b}$$

where $\chi\ell_t$ is the "extrapolation" length.[13] Traditionally an $O(1)$ numerical constant weakly dependent on τ, we prefer to see χ as a free parameter determined by matching diffusion-based results to detailed numerical computations for a significant range of large optical depths. We then seek

$$G_R(t,x,y) = \frac{1}{2}\left[1 + (\chi\ell_t)\frac{\partial}{\partial z}\right]U|_{z=0}. \tag{15}$$

3. MULTIPLE SCATTERING GREEN FUNCTIONS FOR OPAQUE PLANE-PARALLEL MEDIA

3.1 Analytical expression in Fourier/Laplace space

Following standard practice in mathematical physics, this PDE can be (horizontal) Fourier- and (time) Laplace-transformed into an ODE where z is the only independent variable. So we introduce

$$\tilde{U}(s,k_x,k_y;z) = \iiint \exp[-st+i(k_x x+k_y y)]U(t,x,y,z)\,dt dx dy \tag{16}$$

where the semicolon separates the variable and the parameters ("constants") of the resulting 1D problem in z:

$$\tilde{U}'' - \tilde{U}/L^2 = 0, \tag{17}$$

where the single coefficient contains the Fourier-Laplace conjugate variables $k^2 = \|\boldsymbol{k}\|^2 = k_x^2+k_y^2$ and s as well as D:

$$1/L^2 = k^2 + s/D. \tag{18}$$

The boundary/initial conditions in (14a,b) Fourier-Laplace transform into

$$\frac{1}{2}\left[1 - (\chi\ell_t)\frac{d}{dz}\right]\tilde{U}|_{z=0} = 1, \tag{19a}$$

$$\frac{1}{2}\left[1 + (\chi\ell_t)\frac{d}{dz}\right]\tilde{U}|_{z=H} = 0, \tag{19b}$$

for the ODE in Eq. (17). The GF problem now looks exactly like a 2-stream problem for steady and uniform but with an absorption term.[15]

Fourier-Laplace transforms of the boundary flux-field in (15) is the formal counterpart of reflectance in the 2-stream problem; using (15) then (19a), we find

$$\tilde{G}_R(\cdot) = \frac{1}{2}\left[1 + (\chi\ell_t)\frac{d}{dz}\right]\tilde{U}|_{z=0} = \tilde{U}(\cdot;0)-1, \tag{20}$$

where "$\cdot$" stands for $L(s,k)$ and other parameters of the problem. Straightforward algebra leads to

$$\tilde{G}_R(H/L;\chi\ell_t/L) = \frac{1-(\chi\ell_t/L)^2}{1+2(\chi\ell_t/L)/\tanh(H/L)+(\chi\ell_t/L)^2}, \tag{21}$$

equivalently,

$$\tilde{G}_R(\tau_t;\xi(s,k)) = \frac{1-\xi^2}{1+2\xi\,\mathrm{cotanh}(\xi\tau_t/\chi)+\xi^2}, \tag{22}$$

where $\xi = \chi\ell_t/L(s,k)$ is defined in Eq. (18) and

$$\tau_t = (1-g)\tau = H/\ell_t. \tag{23}$$

Figure 2 shows this abstract representation of the reflected GF for a range of rescaled optical depths τ_t; notice the universal behavior at large ξ and the differences at small ξ.

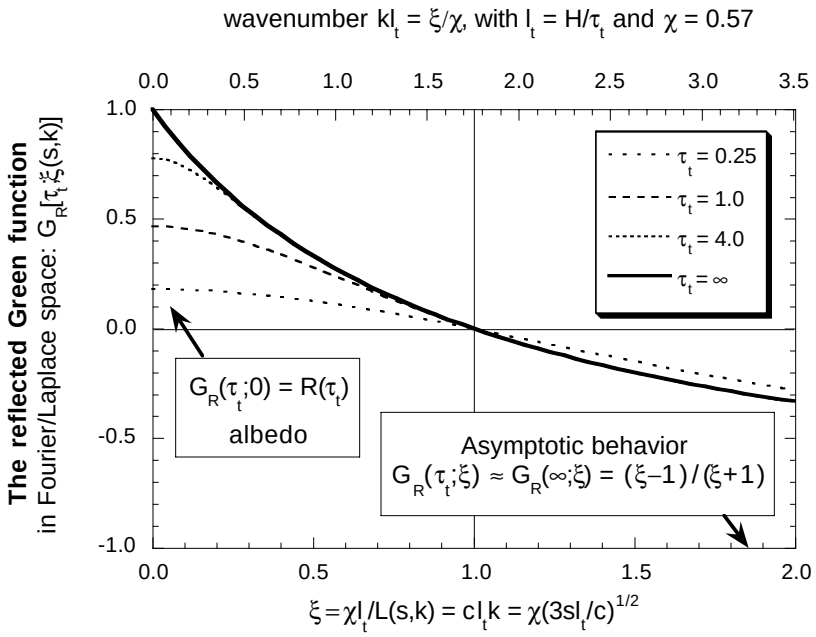

Figure 2: *Radiative Green functions in Fourier/Laplace representation for media of increasing optical depth.* In essence, we vary $H = (1-g)\tau\ell_t$, for fixed ℓ_t. The abcissa represents either Fourier-for-space ($\xi = \chi\ell_t k$) or Laplace-for-time ($\xi = \chi\ell_t\sqrt{s/D} = \chi\sqrt{3s\ell_t/c}$) conjugate variables. Moments of the pathlength λ and horizontal displacement ρ are determined by the small ξ behavior (cf. §3.2).

3.2 Low-order spatial and temporal moments: Dependence on physical parameters

The photon-escape GF in (3) is readily interpreted as the (unconditional) probability of a photon to be reflected from the cloud into any direction at position (x,y) and time t. Conditioned on reflection, we find

$$G_R(t,x,y)\mathrm{d}x\mathrm{d}y\mathrm{d}t \,/\, R = \mathrm{Prob}\{\text{ escape during } [t,t+\mathrm{d}t), \text{ from } [x,x+\mathrm{d}x)\otimes[y,y+\mathrm{d}y) \mid \text{in reflection }\}, \tag{24}$$

where the normalization constant,

$$R = \iiint G_R(t,x,y)\mathrm{d}x\mathrm{d}y\mathrm{d}t, \tag{25}$$

is simply cloud albedo for normal incidence. Analogous relations can be written for transmission (with a subscript "T") where, by conservation, we have $T = 1-R$. Normalized escape GFs can thus be treated as probability density functions and we can compute their moments.

If detailed information about the space/time-dependent bi-directional properties of the cloud's radiative GFs is not available, then we make a standard Lambertian hypothesis:

$$G_R(t,x,y)\mathrm{d}x\mathrm{d}y \approx \pi d_{obs}^2 G_{obs}(t,\theta_\rho,\varphi)\sin\theta_\rho \mathrm{d}\theta_\rho \mathrm{d}\varphi. \tag{26}$$

As shown in the following, the left-hand side can be computed analytically in diffusion theory while the right-hand side requires a numerical approach such as Monte Carlo to avoid the Lambertian assumption.

The simplest in-cloud propagation characteristics of a laser pulse are: mean photon pathlength,

$$\langle\lambda\rangle_R = c\langle t\rangle_R = c\iint dx dy\left[\int t G_R(t,x,y)dt\right] / R; \tag{27}$$

its 2nd-order moment (used in path variance $\langle\lambda^2\rangle_R - \langle\lambda\rangle_R^2$),

$$\langle\lambda^2\rangle_R = c^2\langle t^2\rangle_R = c^2\iint dx dy\left[\int t^2 G_R(t,x,y)dt\right] / R; \tag{28}$$

root-mean-square (rms) horizontal transport $\sqrt{\langle\rho^2\rangle_R}$, where

$$\langle\rho^2\rangle_R = \int dt\left[\iint (x^2+y^2) G_R(t,x,y)dx dy\right] / R \tag{29}$$

which is also the variance of ρ since $\langle x\rangle_R = \langle y\rangle_R = 0$, by symmetry. One can also think of $\langle\rho^2\rangle_R^{1/2}$ as the gyration radius of the spot of diffuse light excited by the laser in cw mode. The main advantage of using low-order moments s that they are the least sensitive to the instrumental or background noise that contaminates measured G_R-values at long times or large distances. Another advantage of using the observables in Eqs. (27–29) is that there is no need for absolute calibration to estimate them from observations using Eqs. (24–26).

The spatial-Fourier/temporal-Laplace solution of the non-steady three-dimensional diffusion equation obtained above for boundary/initial conditions describing a pulsed point-source can be used to compute low-order moments in Eqs. (25) and (27–29). The procedure is standard in probability theory and uses successive derivatives of $\widetilde{G}_R(\tau_t;\xi)$ with respect to ξ at the origin.[6,16] We find:

$$R = \frac{H}{H+2\chi\ell_t} = \frac{(1-g)\tau}{(1-g)\tau+2\chi} \tag{30}$$

for albedo in Eq. (25);

$$\langle\lambda\rangle_R = 2\chi \times H \times [\ 1 + C_{R\lambda}(1,\varepsilon)\ ] \tag{31}$$

for mean pathlength in Eq. (27); and

$$\langle\lambda^2\rangle_R = \frac{4\chi}{5} \times H^2(1-g)\tau \times [\ 1 + C_{R\lambda}(2,\varepsilon)\ ] \tag{32}$$

for the 2nd moment of pathlength in Eq. (28); and

$$\langle\rho^2\rangle_R = \frac{8\chi}{3} \times \frac{H^2}{(1-g)\tau} \times [\ 1 + C_{R\lambda}(1,\varepsilon)\ ] \tag{33}$$

for the variance in horizontal transport defined in Eq. (29). The radiative quantities in (31–33) contain pre-asymptotic correction terms given by:

$$C_{R\lambda}(1,\varepsilon) = C_{R\rho}(2,\varepsilon) = (\varepsilon/2)(1+3\varepsilon/2)/(1+\varepsilon), \tag{34a}$$

$$C_{R\lambda}(2,\varepsilon) = (\varepsilon/2)(8+41\varepsilon/2+75\varepsilon^2/4+\varepsilon^3/8)/(1+\varepsilon)^2; \tag{34b}$$

these corrections become small as

$$\varepsilon = 2\chi/(1-g)\tau = 2\chi\ell_t/H = T/R \tag{35}$$

decreases. Figure 3 shows $T = 1-R$, $\langle\lambda\rangle_R$, $\langle\lambda^2\rangle_R^{1/2}$, and $\langle\rho^2\rangle_R^{1/2}$ from Eqs. (30–35) with $H = 1$ and $\chi = 0.57$ as well as from a Monte Carlo solution of the radiative transfer problem in Eqs. (1–2). Note that, at least for large enough $\tau_t = (1-g)\tau$, knowledge of any two of these quantities enables the retrieval of both H and τ_t. Also, with an observation of R alone and Eq. (30), one can derive rescaled optical depth. This is essentially how cloud optical depths are inferred although, in current procedures, a second wavelength where droplets are absorbing is used simultaneously with a non-absorbing one in a 2-parameter retrieval of τ and of the effective droplet radius.

Representative cloud parameters for a stratus layer are $g = 0.85$, τ in the range 7–70, hence $1 \le (1-g)\tau \le 10$, with H in the corresponding range 300–500 m. Using these values in Fig. 3 leads to an albedo R between 0.6 and 0.9, an rms "spot-size" $\langle\rho^2\rangle_R^{1/2}$ around 300 m, $\langle\lambda\rangle_R \approx$ 500–600 m, and the ratio $\langle\lambda^2\rangle_R^{1/2}/\langle\lambda\rangle_R$ falls between 1.5 and 2. Finally, we note that, apart from exact proportionality constants, the leading terms in Eqs. (31–33) can be obtained from simpler arguments based on the fractal properties of the random walks of the photons in the finite slab that defines the cloud.[5,8,17]

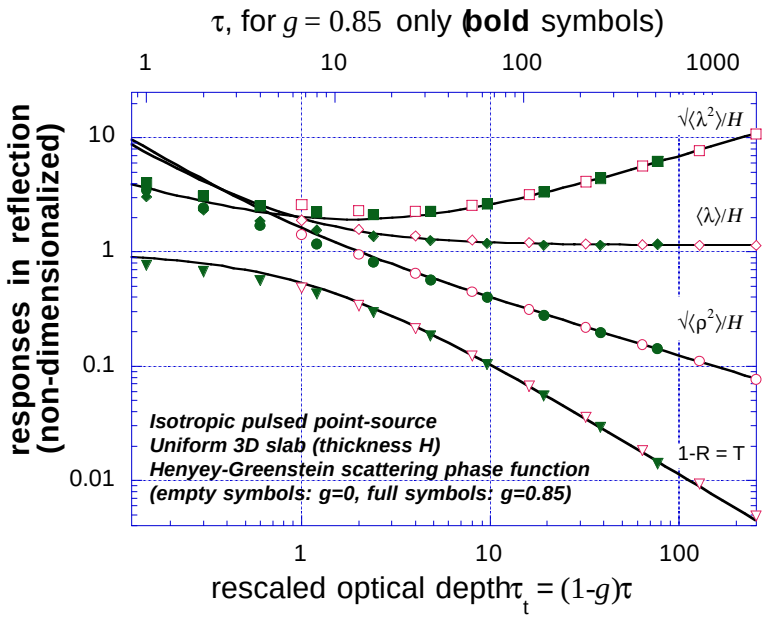

Figure 3: *Four observable quantities in the reflected radiance Green function based on low-order moment analysis versus rescaled cloud optical depth*. From bottom to top at right hand side, we have plotted $1-R$, $\langle\rho^2\rangle_R^{1/2}$, $\langle\lambda\rangle_R$, and $\langle\lambda^2\rangle_R^{1/2}$, from Eqs. (30–35) with $\chi = 0.57$. Monte Carlo results are plotted for both isotropic and forward scattering phase functions; in the latter case, a Henyey-Greenstein[12] model with $g = 0.85$ was used. We note the collapse of the numerical results when they are plotted against $\tau_e = (1-g)\tau$. The agreement with the analytical diffusion results is excellent in the asymptotic ($\tau_e \geq 10$) .regime and reasonably good in the pre-asymptotic ($1 < \tau_e < 10$) region with the correction terms in Eqs. (34a-b).

4. FOUR APPLICATIONS TO CLOUD REMOTE SENSING

4.1 The Nonlocal Independent Pixel Approximation (NIPA)

The operational approach to cloud remote sensing in the solar spectrum is to assume no horizontal variability below the satellite pixel scale and therefore apply locally plane-parallel theory to retrieve one or more physical cloud properties. This practice is sanctioned by NASA's Earth Observing System with such instruments as MODIS on the Terra platform (250-m pixels) where two channels (VIS and NIR) are used to infer cloud optical depth and the effective droplet radius.[18] A similar technique is applied to AVHRR instruments on NOAA platforms (1-km pixels at nadir). This "Independent Pixel Approximation" or IPA[19] has been occasionally[20] applied to instruments with much higher spatial resolution, primarily the TM imager on Landsat (30-m pixels). Finding the limitations of the IPA is clearly an important issue in remote sending.[21]

Davis et al.[8] studied in detail the breakdown of the IPA in essentially unbroken stratocumulus (Sc) layers. This breakdown occurs at small scales due to the 3D radiative transfer process of radiative smoothing[22] and it can easily be diagnosed in the data using wavenumber or wavelet spectra. Marshak et al.[23] offer a way of overcoming this limitation under some circumstances using the Nonlocal Independent Pixel Approximation or "NIPA" in which an "unsmoothing" operator is applied to the radiance field by convolution in Fourier space before invoking the IPA. An acceptable convolution kernel is $1/\tilde{G}_R(k)$ from Eq. (22) and Fig. 2 although in practice Marshak and his co-workers used a simpler expression with in known Fourier-cosine transform pair, at least for variability in one horizontal direction. Specifically, they adopted the symmetric 2-parameter Gamma distribution:

$$G_R(a,\langle|x|\rangle;|x|) = \frac{1}{2\Gamma(a)}\left(\frac{a}{\langle|x|\rangle}\right)^a |x|^{a-1}\exp[-a|x|/\langle|x|\rangle]; \tag{36a}$$

$$\tilde{G}_R(a,\langle|x|\rangle;k) = \cos[a\,\mathrm{atan}(\langle|x|\rangle k/a)] \,/\, [\,1+(\langle|x|\rangle k/a)^2\,]^{a/2}. \tag{36b}$$

In this model, $\langle|x|\rangle$ is the mean horizontal displacement from entry to escape from the medium and $a = \langle|x|\rangle^2/\mathrm{var}(x) = 1/[\langle x^2\rangle/\langle|x|\rangle^2 - 1]$ controls the spread of the GF. Note that $a = 1$ is an exponential GF and in the limit $\langle|x|\rangle \to 0$ we obtain the trivial (no unsmoothing) case of a δ-function at the origin. Numerical simulations suggest values of a somewhat less than unity. Such high-pass filtering is numerically unstable with respect to the presence of noise, so a careful regularization is used to control the fidelity of the outcome in the case-studies and highly recommended in the case of real data. Figure 4 illustrates the outcome of the NIPA procedure.

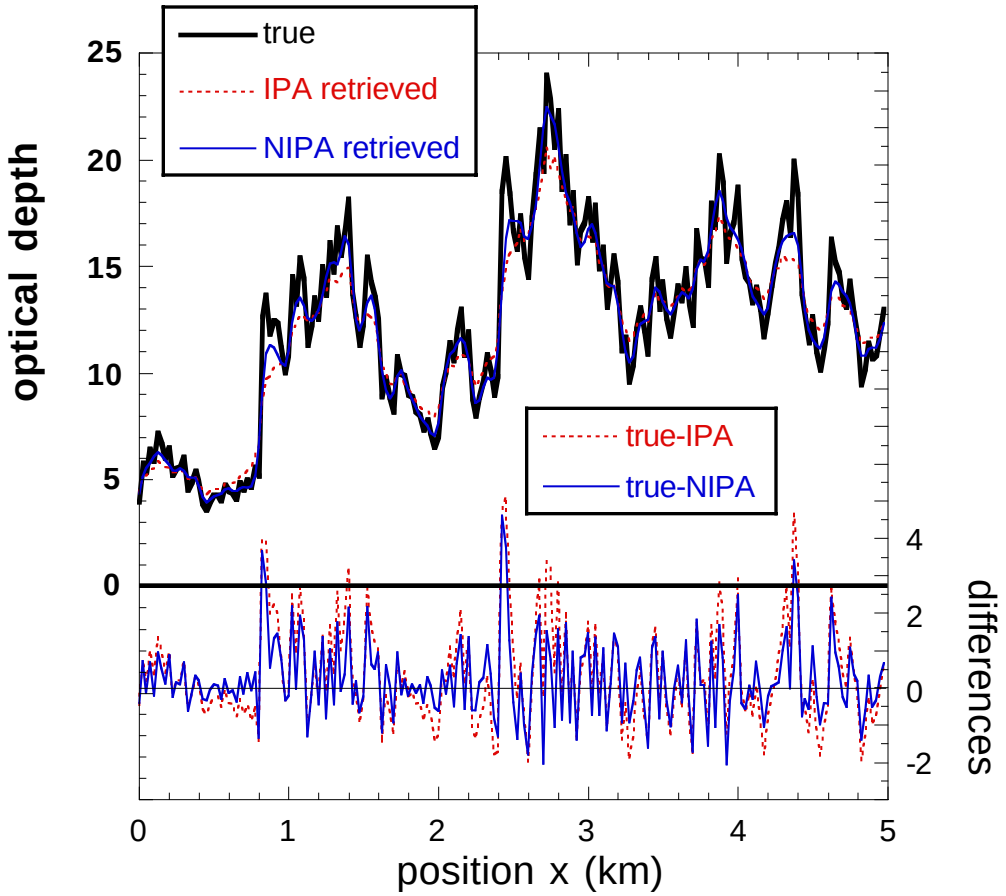

Figure 4: *The Nonlocal Independent Pixel Approximation (NIPA).* A 5-km fragment of the optical depth field retrieved using a standard IPA and a newly developed NIPA. The sun is at zenith. NIPA restores the optical depth variability that would be underestimated by the IPA technique. Note how NIPA sharpens the radiatively smooth field of retrieved optical depths by generating small-scale structure similar to the original optical depth field. For more detailed explanations, see ref. 23.

4.2 The Normalized Difference Cloud Index (NDCI)

In a recent study, Marshak et al.[24] address IPA breakdown in broken cloud fields where the problem is more severe than in Sc due to the enhanced 3D photon transport effects. Focusing on ground-based radiometry from continuous monitoring stations, the authors are lead to define the Normalized Difference Cloud Index or "NDCI." In analogy with the Normalized Vegetation Index (NDVI),[25] this is the difference between down-welling radiances in the near-IR (NIR) and red channels normalized by their sum. On general grounds (linear superposition principle), the radiance field in a cloud/surface system can be expressed as the sum of I_0, the solar-source solution of the RTE for an absorbing surface, and I_ρ a term proportional to the surface albedo ρ which, in the case of green vegetation, is ≈0 in the visible (especially red) and ≈0.5 in the NIR. Now, in the spirit of a NIPA, $I_\rho(x,y;\mathbf{\Omega}=-\mathbf{1}_z)$ can be approximated by a convolution of the $I_0(x,y;\mathbf{\Omega})$ solution, hemispherically integrated to give the down-welling flux $T_0(x,y)$, with the Green function for flux $G_R(x,y) \equiv G_R(\rho)$ associated with a homogeneous cloud and a collimated boundary source, i.e., the integral of Eq. (3) over time. Specifically, we have[26]

$$I_\rho(x,y;\mathbf{\Omega}=-\mathbf{1}_z) \approx \rho \int T_0(x',y') G_R(x-x',y-y') \mathrm{d}x' \mathrm{d}y'. \qquad (37)$$

This convolution product is of course best done in Fourier space using $\widetilde{G}_R(k)$ from (22) or (36b). Since I_0 is essentially independent of wavelength over the red-to-NIR region, the NDCI is reduced to I_ρ for the NIR channel, hence to a knowledge of the reflected Green function. At least in the homogeneous cloud/surface limit, the NDCI is a one-to-one function of cloud optical depth τ at either wavelength. Simulated cloud optical depth retrievals based on the inverse homogeneous NDCI(τ) curve prove to be remarkably accurate in 3D situations, including broken cloud fields. This is explained by the relatively rapid decay of the spatial Green function with horizontal distance at large optical depths. Although not yet fully calibrated, this method is very promising and can potentially be implemented over much of the global aerosol monitoring network AERONET[27] in order to gather a comprehensive climatology of cloud optical depth that will at least complement but may prove more robust than satellite-based efforts. Figure 5 illustrates the outcome of the NDCI algorithm.

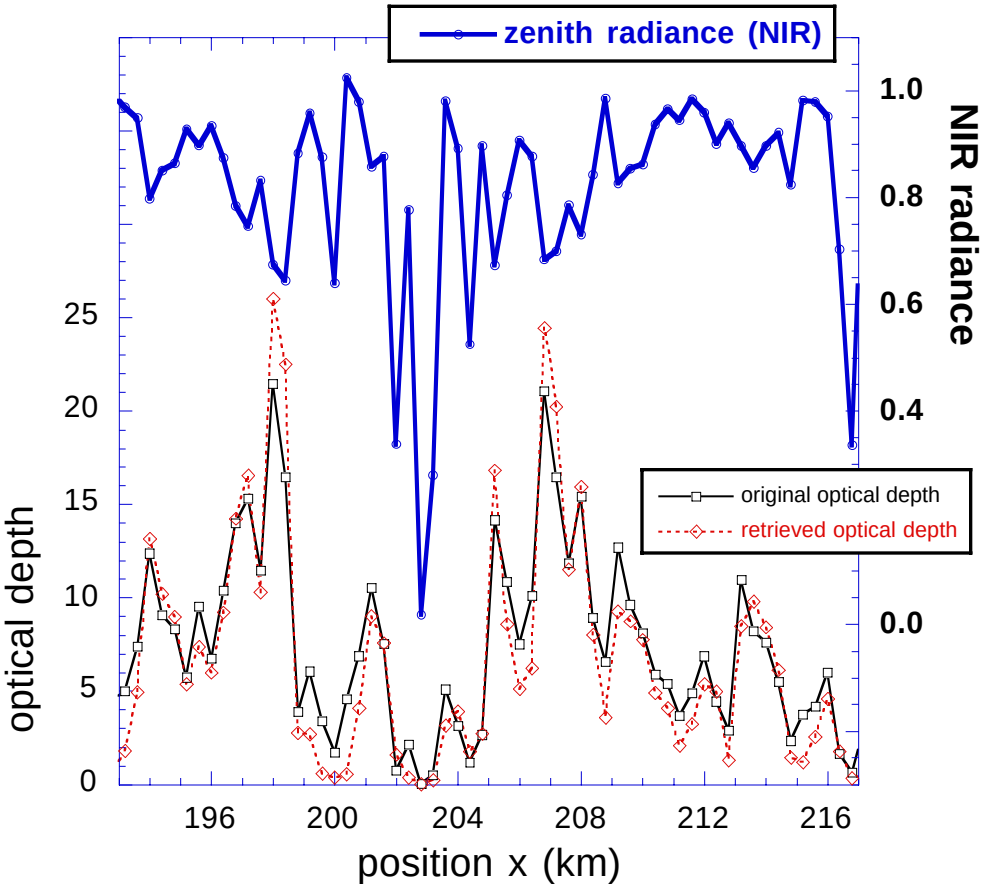

Figure 5: *The Normalized Difference Cloud Index (NDCI).* A 23-km fragment of the original optical depth field and the one retrieved from the NDCI. Zenith radiance indicates a multi-valued character of the problem, e.g., radiances around 198, 200, 205, 208 and 216 km are within 0.20 of 0.68 but they correspond to very different values of optical depth whereas the standard IPA would assign roughly the same value to all these pixels. For more detailed explanations, see ref. 24.

4.3 The Wide-Angle Imaging Lidar (WAIL) prototype system at LANL/NIS-2

The goal of Wide-Angle Imaging Lidar or "WAIL" is simply to observe directly the space-time Green function $G_R(t,\rho)$ illustrated qualitatively and quantitatively in Figs. 1a-b, then investigated theoretically in Sections 2-3. The key component in the instrumental implementation realized at LANL/NIS-2 is the Remote Ultra-Low Light Imager[28] or "RULLI" which is ideally suited for the weak light field far from the impact point of the laser beam at cloud base. However, the sensitivity and time-response characteristics of this detector mandates a flattening of the time-dependent intensity across the focal plane. This is performed with a combination of interference filters, both off and on the laser's wavelength, and an opaque mask at the central portion of the aperture placed up-stream of the pupil. We refer the interested reader to a companion paper by Love et al.[29] in this volume for technical details on the instrumental set-up as well as a successful application of the cloud property retrievals suggested in §3.2 and used below, with inherent limitations, on LITE data. Figure 6 shows a temporal sequence of representative spatial/angular fields captured by the WAIL prototype while observing a relatively opaque cloud above the Fenton Hill Observatory (operated by LANL) in New Mexico.

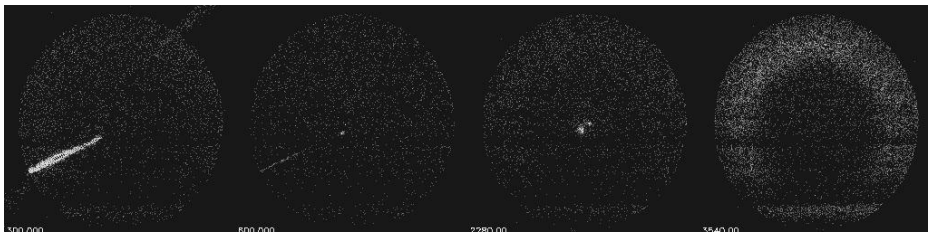

Figure 6: *Four constant-time "slices" in the space-time data-cube produced by WAIL.* An interference filter was used to emphasize the off-beam signal returned from a relatively dense cloud aloft. The complete space-time "movie" can be viewed at the following URL <http://nis-www.lanl.gov/~love/clouds.html>. For more detailed explanations, see ref. 29.

4.4 The returns from a marine stratocumulus layer during the Lidar In-space Technology Experiment (LITE)
The leading terms in Eqs. (30–33) from the diffusion-based and numerically-validated theory presented in Section 3 suggest that any two of these four observables can be used to infer τ and H, given that g varies little in real clouds. Note that using albedo R alone from Eq. (30), i.e., with no spatial or temporal information, can yield only the dimensionless optical depth τ. This is in fact the basic strategy in passive cloud remote sensing in the solar spectrum. However, proper measurement of R calls for an absolute calibration of the passive or active device. We therefore prefer to work with the remaining quantities.

The possibility of using only the two purely temporal quantities defined operationally in Eqs. (27–28) and estimated in the associated diffusion Eqs. (31–32) is particularly interesting for off-beam lidar systems in Low-Earth Orbit (LEO) where it is difficult at best to obtain the radial information used in Eq. (29). We are dealing here the first two moments of the returned pulse shape, independent of exit position.

This remote-sensing strategy can be tested directly with pulse shapes obtained during the shuttle-based LITE mission[30] for the marine Sc case-study, such as illustrated in Fig. 7a. These data were gathered during the night-side of orbit #135 when the large FOV of 3.5 mrad was used in conjunction with the low-gain setting to avoid saturation effects resulting from such highly reflective targets. From the 260 km orbit, this FOV gives a foot-print of 910 m for a beam diameter of 280 m. So ρ is sampled by LITE between 0 and 600 m $\approx$ 2 rms spot-radii from our above estimates based on Eq. (33) and Fig. 3. In this spatial sense, LITE and future space-borne lidar systems with equally wide FOVs are "off-beam;" we will see that, in ground-based and airborne systems with clouds at close range, the same expression has an angular meaning too.

At any rate, we can expect to see very high orders-of-scattering in LITE signals: mean pathlengths $\langle\lambda\rangle_R$ should be $\approx$500–600 m, and rms pathlengths $\langle\lambda^2\rangle_R^{1/2}$ up to twice that much. In particular, this brings in pulse shapes with relatively long multiple-scattering tails; in terms of echo range (cloud-top altitude – extreme pathlength/2), this means that apparent echoes coming from negative altitudes are very likely since cloud-top altitude is $\approx$1 km.

Figure 7a shows four typical non-saturated 532 nm pulse profiles recorded during LITE as a function of both in-cloud pathlength and apparent echo altitude, using the available range information. The multiple-scattering pulse tail is highlighted and the anticipated echoes from below sea level are indeed observed. We must however caution ourselves about predictions based on a cloud model that is assumed homogeneous, vertically as well as horizontally. Horizontal structure is largely smoothed in foot-prints in the range 0.5 to 1 km, at least in marine Sc.[8,22] In sharp contrast, the time-domain signals will be affected by the persistent vertical gradients in liquid water content (LWC) well-documented in the literature.[31] Indeed, the extinction

$$\sigma(z) = 3LWC(z) / 2\rho_w r_e(z), \tag{38}$$

where r_e is effective droplet radius and ρ_w is water density, will be dominated by the change in LWC.

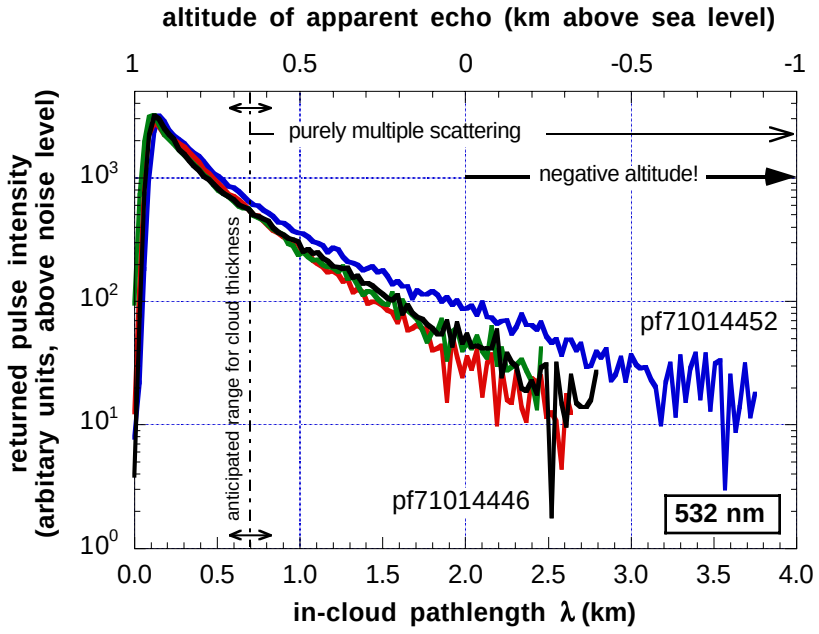

Figure 7a: *Four typical non-saturated LITE returns from a dense marine Sc during orbit #135.*

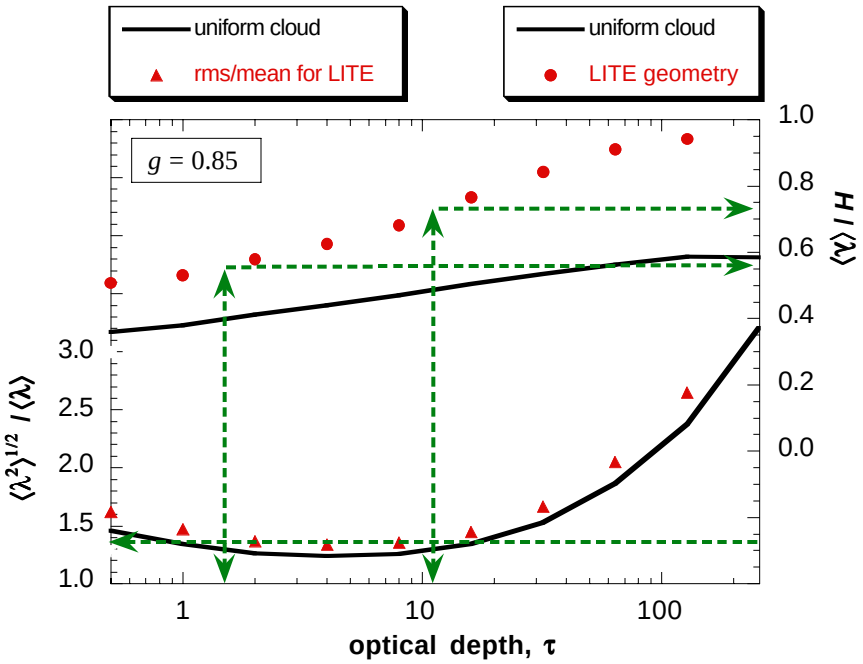

Figure 7b: *Retrieval of optical depth and geometrical thickness of cloud layer using data in Fig. 7a.* See ref. 11 for more details.

We have therefore numerically re-evaluated the radiative quantities in Eqs. (27–28) for cloud models with variable τ that are stratified with a linear increase in $\sigma(z)$ starting from 0 at cloud-base. Figure 7b shows the revised theoretical curves for $\langle\lambda^2\rangle_R^{1/2}/\langle\lambda\rangle_R$ (lower curve and left-hand vertical axis) and $H/\langle\lambda\rangle_R$ (upper curve and readings on the right-hand vertical axis). Noting that the latter is the inverse of $\langle\lambda\rangle_R/H$ in Fig. 3, we see that the new time-domain results (symbols) are systematically smaller that in the homogeneous-cloud case, as expected because the cloud is denser (smaller mean-free-path) in the upper layers that are preferentially probed by the LITE system.

The data in Fig. 7a is used in Fig. 7b in a 2-step cloud-property retrieval scheme. First, the observed $\langle\lambda^2\rangle_R^{1/2}/\langle\lambda\rangle_R$ ratio of 1.38 is used to find a plausible range for the optical depth τ, cf. two intercepts and readings on the horizontal axis. Given the uncertainties in the data and in the theory, "plausible range" is a far better description of the situation than "a choice of two possible values." Then this range in τ is used in conjunction with $\langle\lambda\rangle_R \approx 515$ m to infer a range for H, noting that the higher value of 11 for τ makes more sense than the low value of 1.5 under the present circumstances. However, the inferred range for H is quite narrow anyway. In summary, the data and modeling is consistent with $\tau \approx 10$ and $H \approx 380$ m. Both values are quite reasonable for a nocturnal marine boundary-layer Sc deck.

5. SUMMARY AND OUTLOOK

We surveyed the theory of radiative Green functions for multiple scattering and boundary sources and then demonstrated their relevance to the remote sensing of cloud properties, even in the presence of strong horizontal variability. Both passive (solar) and active (laser radar) approaches were considered, with a special emphasis on space-borne lidar applications for which we used data obtained during NASA's 1994 LITE mission. Because we consider dense (mostly boundary-layer) clouds, we can use the photon diffusion approximation where the theory becomes largely analytical, in turn, this leads to significant insights into the diffusion process.

Several refinements can be made to the procedures presented here, for instance, going from diffuse to collimated sources in the diffusion model and averaging the Green functions over a variability model for optical depth would add more realism to the proposed lidar algorithms. There are also entirely new applications of Green functions, for instance, the higher-order adjoint perturbation theory that is required to compute the radiative response to three-dimensional deviations from horizontal uniformity.[32-34] This is anticipated to be a numerical 3D radiative transfer at once accurate and efficient. As this kind of 3D transport model becomes available, one can start designing fully 3D cloud remote sensing applications and atmospheric correction schemes for land surface remote sensing to remove the contamination of the radiometry by scattered clouds.

ACKNOWLEDGMENTS

This work was supported by the Environmental Sciences Division of U.S. Department of Energy (for AM, under grant DE-A105-90ER61069 to NASA's Goddard Space Flight Center) as part of the Atmospheric Radiation Measurement (ARM) Program. AM acknowledges partial funding for this research from the NASA EOS Project Science Office at the GSFC (under grant NAG5-6675) as part of EOS Validation Program. ABD acknowledges partial funding from LANL's LDRD/ER Program. Both are grateful for discussions with Y. Knyazikhin. RFC acknowledges funding from GSFC's DDF Program.

REFERENCES

1. K. Sassen, "Advances in polarization diversity lidar for cloud remote sensing," *Proc. IEEE* **82**, pp. 1907–1914, 1994.
2. C. M. R. Platt, "Lidar and radiometric observations of cirrus clouds," *J. Atmos. Sci.* **30**, pp. 1191–1204, 1973.
3. L. R. Bissonnette, "Multipe scattering of narrow light beams in aerosols," *Appl. Phys. B* **60**, pp. 315–323, 1995.
4. A. B. Davis, and A. Marshak, "Cloud responses from cw and pulsed lasers as Green's functions: What do they tell us? & Can we measure them?" *8th International Worskshop on MUltiple SCattering Lidar Experiments (MUSCLE 8) Extended Abstract Volume*, L. R. Bissonnette (ed.), pp. 67–71, Def. Res. Est.Valcartier (DREV), Valcartier (Qc), 1996.
5. A. B. Davis, D. M. Winker, A. Marshak, J. D. Spinhirne, R. F. Cahalan, S. P. Love, S. H. Melfi, and W. J. Wiscombe, "Retrieval of physical and optical cloud thicknesses from space-borne and wide-angle lidar," *Advances in Atmospheric Remote Sensing with Lidar*, A. Ansmann et al. (eds.), pp. 193–196, Springer-Verlag, Berlin, 1997.
6. A. B. Davis, R. F. Cahalan, J. D. Spinhirne, M. J. McGill, and S. P. Love, "Off-beam lidar: An emerging technique in cloud remote sensing based on radiative Green-function theory in the diffusion domain," *Phys. Chem. Earth (B)* **24**, pp. 757–765, 1999.
7. A. Yodh, and B. Chance, "Spectroscopy/imaging with diffusing light," *Phys. Today* **48**, pp. 34–40, 1995.
8. A. B. Davis, A. Marshak, R. Cahalan, and W. Wiscombe, "The LANDSAT scale-break in stratocumulus as a three-dimensional radiative transfer effect, implications for cloud remote sensing," *J. Atmos. Sci.* **54**, pp. 241–260, 1997.
9. D. M. Winker, "Simulation and modeling of the multiple scattering effects observed in LITE data," *Advances in Atmospheric Remote Sensing with Lidar*, A. Ansmann et al. (eds.), pp. 185–188, Springer-Verlag, Berlin, 1997.
10. S. D. Miller, and G. L. Stephens, "Multiple scattering effects in the lidar pulse stretching problem," *J. Geophys. Res.* **104**, pp. 22205–22219, 1999.
11. A. B. Davis, D. M. Winker, M. A. Vaughan, and R. F. Cahalan, "First retrievals of dense cloud properties from off-beam/multiple-scattering lidar data collected in space," *Laser Remote Sensing of the Atmosphere: Selected Papers from the 20th International Conference on Laser Radar*, A. Dabas and J. Pelon (eds.), École Polytechnique, Palaiseau (France), 2001 (in press).
12. L. C. Henyey, and J. L. Greenstein, "Diffuse radiation in the galaxy," *Astrophys. J.* **93**, pp. 70–83, 1941.
13. K. M. Case, and P. F. Zweifel, *Linear Transport Theory*, Addison–Wesley Publ. Co., Reading (Ma), 1967.
14. F. Rief, *Fundamentals of Statistical and Thermal Physics*, McGraw-Hill, New York (NY), 1965.
15. W. E. Meador, and W. R. Weaver, "Two-stream approximations to radiative transfer in planetary atmospheres: A unified description of existing methods and a new improvement," *J. Atmos. Sci.* **37**, pp. 630–643, 1980.
16. W. Feller, *An Introduction to Probability Theory and its Applications*, 2 vols., Wiley, New York (NY), 1971.
17. A. B. Davis, "Physical thickness and optical depth of stratocumulus from space-borne lidar, a moment-based diffusion method," *Technical Digest of OSA Topical Meeting on "Optical Remote Sensing of the Atmosphere"*, June 21–25, 1999, Santa Barbara (Ca), pp. 66–68, Optical Society of America, Washington (DC), 1999.
18. T. Y. Nakajima, and M. D. King, "Determination of the optical thickness and effective particle radius of clouds from reflected solar radiation measurements – Part I, Theory," *J. Atmos. Sci.* **47**, pp. 1878–1893, 1990.
19. R. F. Cahalan, W. Ridgway, W. J. Wiscombe, S. Gollmer, and Harshvardhan, "Independent pixel and Monte Carlo estimates of stratocumulus albedo," *J. Atmos. Sci*. **51**, pp. 3776–3790, 1994.
20. H. W. Barker, B. A. Wielicki, and L. Parker, "A parameterization for computing grid-averaged solar fluxes for inhomogeneous marine boundary layer clouds – Part 2, Validation using satellite data," *J. Atmos. Sci.* **53**, pp. 2304–2316, 1996.
21. L. Chambers, B. A. Wielicki, and K. F. Evans, "On the accuracy of the independent pixel approximation for satellite estimates of oceanic boundary layer cloud optical depth," *J. Geophys. Res.* **102**, 1pp. 779–1794, 1997.
22. A. Marshak, A. B. Davis, W. J. Wiscombe, and R. F. Cahalan, "Radiative smoothing in fractal clouds," *J. Geophys. Res.* **100**, pp. 26247–26261, 1995.
23. A. Marshak, A. B. Davis, R. F. Cahalan, and W. J. Wiscombe, "Nonlocal independent pixel approximation: Direct and inverse problems," *IEEE Trans. Geosc. and Remote Sens*. **36**, pp. 192–205, 1998.
24. A. Marshak, Y. Knyazikhin, A. B. Davis, W. J. Wiscombe, and P. Pilewskie, "Cloud – vegetation interaction: Use of Normalized Difference Cloud Index for estimation of cloud optical thickness," *Geophys. Res. Lett.* **27**, pp. 1695–1698, 2000.

25. C. J. Tucker, "Red and photographic infrared linear combination for monitoring vegetation," *Remote Sens. Environ.* **8**, pp. 127–150, 1979.
26. Y. Knyazikhin, and A. Marshak, "Mathematical aspects of BRDF modeling: Adjoint problem and Green's function," *Remote Sens. Review* **18**, pp. 263-280, 2000.
27. B. N. Holben, and 12 co-authors, "AERONET - A federated instrument network and data archive for aerosol characterization," *Remote Sens. Environ.* **66**, pp. 1–16, 1998.
28. W. C. Priedhorsky, R. C. Smith, and C. Ho, "Laser ranging and mapping with a photon-counting detector," *Appl. Opt*. **35**, pp. 441–452, 1996.
29. S. P. Love, A. B. Davis, C. A. Rohde, and C. Ho, "Wide-Angle Imaging Lidar (WAIL): A ground-based instrument for monitoring the thickness and density of optically thick clouds," in *S.P.I.E. Proceedings*, *vol. 4377: "Laser Radar Technology and Applications VI,"* G. W. Kamerman (ed.), 2001 (this volume).
30. D. M. Winker, R. H. Couch, and M. P. McCormick, "An overview of LITE: NASA's Lidar In-space Technology Experiment," *Proc. IEEE* **84**, pp. 164–180, 1996.
31. J.–L. Brenguier, "Parameterization of the condensation process: A theoretical approach," *J. Atmos. Sci*. **48**, pp. 264–282, 1991.
32. S. A. W. Gerstl, and W. M. Stacey, Jr., "A class of second-order approximate formulations of deep penetration radiation transport problems," *Nucl. Sci. Eng*. **51**, pp. 339–343, 1973.
33. M. A. Box, M. Keevers, and B. H. J. McKellar, "On the perturbation series for radiative effects," *J. Quant. Spect. Rad. Trans*. **39**, pp. 219–223, 1988.
34. M. A. Box, S. A. W. Gerstl, and C. Simmer, "Computation of atmospheric radiative effects via perturbation theory," *Beitr. Phys. Atmosph.* **62**, pp. 193–199, 1989.